

Late-twentieth-century emergence of the El Nino propagation asymmetry and future projections

Author:

Santoso, Agus; McGregor, Shayne; Jin, F; Cai, W; England, Matthew; An, S; McPhaden, M; Guilyardi, E

Publication details:

Nature

v. 504

Chapter No. 7478

pp. 126-130

0028-0836 (ISSN)

Publication Date:

2013

Publisher DOI:

<http://dx.doi.org/10.1038/nature12683>

License:

<https://creativecommons.org/licenses/by-nc-nd/3.0/au/>

Link to license to see what you are allowed to do with this resource.

Downloaded from <http://hdl.handle.net/1959.4/53704> in <https://unsworks.unsw.edu.au> on 2024-04-19

Late 20th Century Emergence of El Niño Propagation Asymmetry and Future Projections

***Agus Santoso^{1,2}, Shayne McGregor^{1,2}, Fei-Fei Jin³, Wenju Cai⁴, Matthew H. England^{1,2}, Soon-Il An⁵, Michael J. McPhaden⁶, Eric Guilyardi^{7,8}**

1. Climate Change Research Centre, University of New South Wales, Sydney, Australia
2. ARC Centre of Excellence for Climate System Science, University of New South Wales, Sydney, Australia
3. Department of Meteorology, University of Hawaii at Manoa, Honolulu, United States
4. CSIRO Marine and Atmospheric Research, Aspendale, Melbourne, Australia
5. Department of Atmospheric Sciences, Yonsei University, Seoul, Korea
6. NOAA/Pacific Marine Environmental Laboratory, Seattle, Washington 98115, USA
7. LOCEAN/IPSL, CNRS, Paris, France
8. NCAS-Climate, University of Reading, UK

*Agus Santoso: a.santoso@unsw.edu.au

Shayne McGregor: shayne.mcgregor@unsw.edu.au

Fei-Fei Jin: iff@hawaii.edu

Wenju Cai: wenju.cai@csiro.au

Matthew H. England: m.england@unsw.edu.au

Soon-Il An: sian@yonsei.ac.kr

Michael J. McPhaden: michael.j.mcphaden@noaa.gov

Eric Guilyardi: eric.guilyardi@locean-ipsl.upmc.fr

27 The El Niño Southern Oscillation (ENSO) is Earth's most prominent source of
28 interannual climate variability, exerting profound worldwide impacts¹⁻⁷. Despite
29 decades of research, its behavior continues to challenge scientists. During La Niña and
30 modest El Niño, sea surface temperature (SST) anomalies propagate westward along
31 the equatorial Pacific, similar to the seasonal cycle⁷. In stark contrast, SST anomalies
32 propagate eastward during extreme El Niño, prominently in the post-1976 period⁷⁻¹⁰,
33 spurring highly unusual weather events worldwide with costly consequences^{3-6,11}. The
34 cause of this propagation asymmetry is currently unknown¹⁰. Here we trace the cause
35 to an asymmetry in the upper ocean circulation in the equatorial Pacific, whereby the
36 westward flowing currents are enhanced during La Niña but reversed during extreme
37 El Niño events. Our results highlight that propagation asymmetry is favored when the
38 westward mean equatorial currents weaken, as projected under global warming¹²⁻¹⁴. By
39 analysing past and future climate simulations, we find that an aggregate of models that
40 exhibit more realistic propagation indeed simulate a doubling in the occurrences of El
41 Niño events that feature prominent eastward propagation characteristics in a warmer
42 world. Our analysis thus suggests that more frequent emergence of propagation
43 asymmetry will be a symptom of a warming planet.

44 The tropical Pacific is home to intense convection, allowing for strong thermal and dynamical
45 interactions between the upper ocean and the overlying atmosphere¹⁵. As warm SST
46 anomalies propagate eastward during extreme El Niño events (e.g., 1982/83, 1997/98;
47 Extended Data Fig. 1a) non-linear dynamical heating processes tend to intensify the
48 anomalously warm SST⁹, while the western Pacific warm pool (water with temperature
49 greater than 28°C) extends eastward, moving the eastern edge of the warm pool beyond
50 160°W. This induces an eastward shift of equatorial rainfall and an extreme swing of the
51 Southern Hemisphere's largest rainband, the South Pacific Convergence Zone¹¹, causing

52 extreme hydroclimatic conditions that most severely impact vulnerable island countries in the
 53 Pacific^{11,16}. Beyond the Pacific, virtually every continent felt the impacts of the drastic shift
 54 in weather patterns during the 1982/83 extreme El Niño, and in the U.S. alone crop losses
 55 were estimated to be around \$10–12 billion⁴ (approximately \$24-26 billion in 2013 dollars).
 56 These profound impacts demand an improved understanding of ENSO propagation dynamics.
 57 Many studies have evaluated the relative importance of various ocean-atmosphere feedback
 58 processes¹⁷⁻¹⁹, yet the mechanism for the propagation asymmetry remains unresolved. Here
 59 we show that an asymmetry in the zonal flow along the equatorial Pacific upper ocean
 60 (hereafter referred to as equatorial Pacific current) is the main cause.
 61 Utilizing various observational data assimilation systems (see Methods and Supplementary
 62 Table 1), we quantify the propagation characteristics of temperature anomalies (T') by
 63 compositing the equatorial warming and cooling rates (time derivative of temperature, T_t') of
 64 the surface mixed layer for the strongest El Niño events on record (1982/83 and 1997/98, Fig.
 65 1a) and all La Niña events (Fig. 1b) since 1976. The composite covers the evolution over a
 66 two-year period, before and after the event peak (approximately in January; Jan (1)). The
 67 contour of $T_t'=0$ marks the peak of the temperature anomaly (dashed curve, Figs. 1a and b).
 68 A linear regression using the samples of zero-value rates is constructed (green line). The
 69 slope (β) describes the propagation characteristics: a positive slope indicating temperature
 70 anomalies peak earlier in the west, i.e., eastward propagation; a negative slope indicating
 71 westward propagation; and the greater the amplitude, the slower the propagation. This
 72 analysis shows opposite zonal propagation of SST anomalies between these two types of
 73 events; eastward during extreme El Niño ($\beta=0.82$) and westward during La Niña ($\beta=-0.46$).
 74 During moderate El Niño the propagation is westward (Extended Data Fig. 1b), similar to La
 75 Niña.

76 The direction of propagation has been understood as arising from three main competing
 77 positive feedback processes^{17,18}. The zonal advective and Ekman pumping feedbacks
 78 associated with fluctuations in the Trade Winds involve advection of climatological SST
 79 along the equator by anomalous zonal currents (u') and upwelling (w')^{20,21}, respectively (i.e.,
 80 $u'\bar{T}_x$ and $w'\bar{T}_z$; overbar indicates climatological mean, prime indicates anomaly, and subscript
 81 indicates gradient along a specified direction). The thermocline feedback involves vertical
 82 advection ($\bar{w}T'_z$) associated with eastward propagating internal waves which influence SST in
 83 the eastern Pacific through the mean upwelling (\bar{w}) of water at the thermocline (a narrow
 84 depth range of strong vertical temperature gradients below the mixed layer). These processes
 85 can establish propagation of SST anomalies in either direction: eastward if the thermocline
 86 feedback dominates, and westward otherwise¹⁷. Linear theories have highlighted a higher
 87 importance of the thermocline feedback in the decades since the mid-1970s^{8,22,23}; this would
 88 however predict an eastward propagation during La Niña events as well¹⁹, in contrast to
 89 observations¹⁰ (Fig. 1b).

90 La Niña anomalies can be viewed as an enhancement of the prevailing climate, with stronger
 91 westward flowing surface currents. On the other hand, eastward current anomalies during El
 92 Niño associated with anomalously weak Trade Winds²⁴ (Extended Data Fig. 2), oppose and
 93 even exceed in amplitude the background current, leading to a net eastward flow (Fig. 1c).
 94 This asymmetry in the total zonal current is apparent in all reanalyses (Extended Data Fig. 3,
 95 Supplementary Tables 2 and 3). Our heat budget analysis (see Methods) shows that advection
 96 of anomalous temperature by the total current, $(\bar{u} + u')T'_x$, which is strongly westward during
 97 La Niña but eastward during extreme El Niño (Fig. 1c; Extended Data Fig. 4), represents one
 98 salient asymmetric feature that should be considered.

99 We therefore examine how the mixed-layer heat balance changes when the total current-
100 induced heat flux $((\bar{u} + u')T'_x)$ is removed from the heat-budget equation (see Methods).
101 Evolution of the residual warming and cooling rates shows that without the effect of the total
102 current, an eastward propagation would result for extreme El Niño and La Niña (red dashed
103 line in Figs 2a and b), both with a positive slope of β^* , 0.55 and 0.69, respectively. This
104 reconstructs a linear framework in which the thermocline feedback dominates, leading to an
105 eastward propagation for all events after 1976¹⁹. Thus it is the westward total flow that plays
106 a key role in determining the westward propagation during La Niña.

107 The role of the total current can be further understood by decomposing it into one component
108 that is due to the long-term mean current $(\bar{u}T'_x)$ and another due to the ENSO-related current
109 anomaly $(u'T'_x)$. We find that the westward long-term mean current favours a westward
110 propagation during both types of events; without it the eastward propagation during extreme
111 El Niño is more prominent and the propagation during La Niña reverses to eastward (red
112 dashed line, Extended Data Figs 1d and e). The current anomaly, on the other hand, has an
113 opposite effect on the two types of events (Supplementary Table 4). Without the effect of the
114 eastward current anomaly, the eastward tendency during extreme El Niño is severely
115 weakened (red dashed line in Fig. 2c). This eastward anomalous current, stronger than the
116 westward mean current, leads to a flow reversal during extreme El Niño (Fig. 1c), making the
117 eastward propagation characteristic more prominent (Fig. 2a). During La Niña on the other
118 hand, the anomalous current reinforces the effect of the westward mean flow for a more
119 pronounced westward propagation (Extended Data Fig. 1e, Figs. 2b, d). During moderate El
120 Niño events, the eastward current anomaly is far weaker than the mean current, and thus the
121 total current remains westward (Fig. 1c, Extended Data Fig. 1c). Thus, for moderate ENSO
122 events, there is no asymmetry, and SST anomalies for both El Niño and La Niña propagate
123 westward (Supplementary Table 4).

The non-linear effect is more prominent post-1976 (Supplementary Table 4) when El Niño events are stronger^{9,25} with large eastward current anomalies that are occasionally comparable to, or greater than, the mean background current (Fig. 1c). During such events, this effect reinforces eastward propagation induced by the thermocline feedback. During La Niña, the westward current, along with the zonal advective and Ekman pumping feedbacks, weakens the thermocline feedback effect, resulting in a net westward propagation (Fig. 3). This superposition of ENSO-related large current anomalies onto the long-term mean westward current invalidates the assumptions of linearity, making linear theories unable to explain the propagation asymmetry.

Thus, interplay between the ENSO-related current anomaly and the climatological current determines the way the equatorial Pacific circulation influences zonal propagation of SST anomalies. This means that a change in ENSO intensity or in the mean current can influence the extent to which the propagation asymmetry can be observed. The post-1976 prominence of the propagation asymmetry is partly because of the extremity of the 1982/83 and 1997/98 El Niños. The mean current itself weakened through the 1980-2000 period (dashed curve, Fig. 1c), with a consistent weakening of the Trade Winds (Extended Data Fig. 2b). Although this mean current reduction could be interpreted as a rectification of a change in ENSO variability^{26,27}, a weakened mean current will favour occurrences of an eastward propagation, even if El Niño intensity does not change. Presently there is no agreement among climate models on the magnitude of future ENSO^{28,29}. However, the consensus that emerges is a future with weaker equatorial mean westward currents¹²⁻¹⁴. Our study implies that this would increase the likelihood for occurrences of El Niños with prominent eastward propagation characteristics.

To this end, we analyze 40 climate models that participated in the Coupled Model Intercomparison Project phases 3 and 5 (CMIP3 and CMIP5), subject to increasing

atmospheric CO₂ concentration (see Methods). With the large number of simulated ENSO events, the multi-model aggregate demonstrates robust statistics reaffirming the above conclusion that weaker mean currents and current reversals, which are projected to be of a more typical future condition, are conducive for eastward propagation (see Methods and Extended Data Figs. 5-7). Indeed, we find that a subset of models that are more realistic in terms of flow features and frequency of El Niño events with prominent eastward propagation (19 models; see Methods and Extended Data Figs. 8-10 for model selection), simulate a 100% aggregate increase in the mean occurrence of such events (Fig. 4a), from about 2.7 events in 1907-1999 to about 5.4 events in 2006-2098.

The role of the current is further highlighted as the increase in eastward propagating events is skewed toward weaker mean currents (Fig. 4b; Extended Data Fig. 10b), and this occurs for El Niño events of all magnitude (Fig. 4c). There is, in particular, a tendency for the increase to be larger in models that project stronger ENSO amplitude (Extended Data Fig. 10c), which is in turn associated with more occurrences of a current reversal (Extended Data Fig. 10d), a feature unique to the 1982/83 and 1997/98 El Niños. Stratifying the statistics (Fig. 4c) in terms of a current reversal or otherwise, 45% of the increase is found to be associated with current reversals, most of which are El Niños stronger than the typical magnitude of past events (Fig. 4d). However, the inter-model consensus for ENSO amplitude projection is weak, despite a reduced mean current in all models (Extended Data Figs. 10b and c). This suggests that a weakened mean current is the determining factor for future increases in eastward propagating events of all magnitudes, including extreme El Niños, either through the thermocline feedback effect or a current reversal, or both.

In summary, while different factors have been proposed to explain various non-linear characteristics of ENSO^{9,25,30}, none have been found to explain the cause for its propagation asymmetry seen in recent decades. Here we have provided observational and modelling

evidence that the equatorial Pacific current is an important element for this asymmetry. The superposition of a current anomaly during ENSO onto the long-term mean westward flow enhances the westward currents during La Niña, but reverses the currents during extreme El Niño. The role of the equatorial currents highlighted here casts a fresh perspective on the fundamentals of ENSO behaviour. Given the projected weakening of the background mean flow under global warming, our analysis not only resolves a perplexing scientific issue, but suggests that increased occurrences of ENSO propagation asymmetry will be a manifestation of greenhouse warming with important socioeconomic consequences.

METHODS SUMMARY

The propagation tendency of temperature anomalies during ENSO events is quantified as the slope of the zero-value contour of warming and cooling rates on ENSO time scales that tracks the peak of temperature anomalies as they evolve in time along the equatorial Pacific (Figs. 1a, 1b). A positive (negative) slope in the time-longitude space indicates eastward (westward) propagating temperature anomalies: the steeper the slope the slower the zonal propagation and thus the more observable the propagation characteristic. To investigate the factors that can cause temperature anomalies to propagate zonally, we conduct a heat budget analysis of the ocean surface mixed layer. All variables are derived from five ocean reanalysis systems that assimilate high quality observational products going back to 1980 or earlier (Supplementary Table 1). Our surface heat balance explicitly expresses the zonal advection of temperature anomaly by the mean current and is viewed to interact with the non-linear component (i.e., advection by anomalous current). Removing certain heat-flux components from the heat balance would alter the slope of the zero-value contour, and so by comparing the altered slope (β^*) with the original (β) its influence on the propagation can be inferred. Because this study concerns asymmetry between El Niño and La Niña, a composite approach is adopted (see Methods for classification of ENSO events). The implication of our

results for future climate is assessed through analysis of forty CMIP3 and CMIP5 climate models (see full Methods).

Online Content Any additional Methods, Extended Data display items, Source Data, and Supplementary Information are available in the online version of the paper; references unique to these sections appear only in the online paper.

References

1. McPhaden, M. J., Zebiak, S.E. & Glantz, M. H. ENSO as an integrating concept in Earth science. *Science* **314**, 1740-1745 (2006).
2. Lehodey, P., Bertignac, M., Hampton, J., Lewis, A. & Picaut, J. El Niño Southern Oscillation and tuna in the western Pacific. *Nature* **389**, 715-718 (1997).
3. Bove, M. C., O'Brien, J. J., Eisner, J. B., Landsea, C. W. & Niu, X. Effect of El Niño on U.S. landfalling hurricanes, revisited. *Bull. Amer. Meteor. Soc.* **79**, 2477–2482 (1998).
4. Wilhite, D. A., Wood, D. A. & Meyer, S. J. Climate-related impacts in the United States during the 1982–83 El Niño. *Climate Crisis*, M. Glantz, R. Katz, and M. Krenz, Eds., UNEP, 75–78 (1987).
5. Changnon, S. A., Impacts of 1997–98 El Niño generated weather in the United States. *Bull. Amer. Meteor. Soc.* **80**, 1819–1827 (1999).
6. Liu, Z. & Alexander, M. Atmospheric bridge, oceanic tunnel, and global climatic teleconnections. *Rev. Geophys.* **45**, RG2005, <http://dx.doi.org/10.1029/2005RG000172> (2007).
7. Wallace, J. M. *et al.* On the structure and evolution of ENSO-related climate variability in the tropical Pacific: Lessons from TOGA. *J. Geophys. Res.* **103**, 14241-14259 (1998).
8. Wang, B. & An, S.-I. A mechanism for decadal changes of ENSO behaviour: roles of background wind changes. *Clim. Dyn.* **18**, 475-486 (2002).

- 224 9. An, S.-I. & Jin, F.-F. Nonlinearity and asymmetry of ENSO. *J. Climate* **17**, 2399-2412
225 (2004).
- 226 10. McPhaden, M. J. & Zhang, X. Asymmetry in zonal phase propagation of ENSO sea
227 surface temperature anomalies. *Geophys. Res. Lett.* **36**, L13703,
228 <http://dx.doi.org/10.1029/2009GL038774> (2009).
- 229 11. Cai, W. *et al.* More extreme swings of the South Pacific convergence zone due to
230 greenhouse warming. *Nature* **488**, 365-369 (2012).
- 231 12. Vecchi, G. A. *et al.* Weakening of tropical Pacific atmospheric circulation due to
232 anthropogenic forcing. *Nature* **441**, 73-76 (2006).
- 233 13. DiNezio, P. *et al.* Climate response of the equatorial Pacific to global warming. *J.*
234 *Climate* **22**, 4873-4892 (2009).
- 235 14. Sen Gupta, A., Ganachaud, A., McGregor, S., Brown, J. N. & Muir, L. Drivers of the
236 projected changes to the Pacific Ocean equatorial circulation. *Geophys. Res. Lett.* **39**,
237 L09605, <http://dx.doi.org/10.1029/2012GL051447> (2012).
- 238 15. Graham, N. E., & Barnett, T. P. Sea surface temperature, surface wind divergence, and
239 convection over tropical oceans. *Science* **238**, 657-659 (1987).
- 240 16. Vincent, E. M. *et al.* Interannual variability of the South Pacific Convergence Zone and
241 implications for tropical cyclone genesis. *Clim. Dyn.* **36**, 1881-1896 (2011).
- 242 17. Neelin, D. J. *et al.* ENSO theory. *J. Geophys. Res.* **103**, 14261-14290 (1998).
- 243 18. Jin, F.-F., & Neelin, J. D. Modes of interannual tropical ocean-atmosphere interaction – a
244 unified view. Part I: Numerical results. *J. Atmos. Sci.* **50**, 3477-3503 (1993).
- 245 19. Fedorov, A., & Philander, S. G. H. A stability analysis of tropical ocean-atmosphere
246 interactions: Bridging measurements and theory for El Niño. *J. Climate* **14**, 3086-3101
247 (2001).

- 248 20. An, S.-I., Jin, F.-F. & Kang, I.-S. The role of zonal advection feedback in phase
249 transition and growth of ENSO in the Cane-Zebiak model. *J. Met. Soc. Japan* **77**, 1151-
250 1160 (1999).
- 251 21. Kang, I.-S., An, S.-I. & Jin, F.-F. A systematic approximation of the SST anomaly
252 equation for ENSO. *J. Met. Soc. Japan* **79**, 1-10 (2001).
- 253 22. An, S.-I. & Jin, F.-F. An eigenanalysis of the interdecadal changes in the structure and
254 frequency of ENSO mode. *Geophys. Res. Lett.* **27**, 1573-2576 (2000).
- 255 23. Fedorov, A., & Philander, S. G. H. Is El Niño changing? *Science* **288**, 1997-2002 (2000).
- 256 24. Siedel, H., & Giese, B. S. Equatorial currents in the Pacific Ocean 1992-1997. *J.*
257 *Geophys. Res.* **104**, 7849-7863 (1999).
- 258 25. Jin, F.-F., An, S.-I., Timmermann, A. & Zhao, J. Strong El Niño events and nonlinear
259 dynamical heating. *Geophys. Res. Lett.* **30**, 1120, [http://dx.doi.org/10.1029/](http://dx.doi.org/10.1029/2002GL016356)
260 2002GL016356 (2003).
- 261 26. Choi, J., An, S.-I., Dewitte, B. & Hsieh, W. W. Interactive feedback between the tropical
262 Pacific decadal oscillation and ENSO in a coupled general circulation model. *J. Climate*
263 **22**, 6597-6611 (2009).
- 264 27. Liang, J., Yang, X.-Q., & Sun, D.-Z. The effect of ENSO events on the tropical Pacific
265 mean climate: Insights from an analytical model. *J. Climate* **25**, 7590-7606 (2012).
- 266 28. Guilyardi, E., El Niño-mean state-seasonal cycle interactions in a multi-model ensemble.
267 *Clim. Dyn.* **26**, 329-348 (2006).
- 268 29. Collins, M. *et al.* The impact of global warming on the tropical Pacific Ocean and El
269 Niño. *Nat. Geosci.* **3**, 391-397 (2010).
- 270 30. Frauen, C. & Dommenges, D. El Niño and La Niña amplitude asymmetry caused by
271 atmospheric feedbacks. *Geophys. Res. Lett.* **37**, L18801, doi: 10.1029/2010GL044444
272 (2010).

Acknowledgements The authors thank Drs Francia Avila and Jules Kajtar for downloading and processing the climate models datasets. A.S., S.M., and M.H.E. are supported by the Australian Research Council. W.C. is supported by the Australian Climate Change Science Programme. S.-I.A. was supported by the National Research Foundation of Korea Grant funded by the Korean Government (MEST) (NRF-2009-C1AAA001-2009-0093042). M.J.M. is supported by NOAA. This is PMEL contribution no. 3977.

Author Contributions A.S. and S.M. conceived the study in discussion with F.-F.J. A.S. designed and conducted the analysis. W.C. and A.S. wrote the initial draft of the paper. All authors contributed to interpreting results, presentation, and improvement to the paper.

Author Information Reprints and permissions information is available at www.nature.com/reprints. The authors declare no competing financial interests. Correspondence and requests for materials should be addressed to A.S. (a.santoso@unsw.edu.au)

Figure legends

Figure 1 | Equatorial Pacific current and zonal propagation of ENSO SST anomalies. a, Warming and cooling rate (color shades; in unit of °C per month) of the equatorial Pacific surface mixed layer on interannual time scales (an average over 5°S-5°N) composited over extreme El Niño (1982, 1997) lifecycle across all reanalysis products. Red (blue) contours indicate the associated positive (negative) SST anomalies. Statistically significant values at the 95% confidence level are shaded and contoured. **b,** As in **a** but for post-76 La Niña events. The mean of the linear-fit slope (green line) of the phase transition (dashed black line), β (in unit of seconds per meter), across the products is 0.82 in **a** and -0.45 in **b**, both significant above the 95% confidence level ($P < 0.05$). **c,** Zonal current velocity averaged

across the reanalysis products, over 5°S-5°N, 160°E-90°W, and over August to December. Dashed curve highlights interdecadal variation using a 13-year running mean. Gray shading denotes two standard deviation about each mean value, representing monthly spread and variations across reanalyses. Red and blue filled circles indicate occurrences of strong El Niño and La Niña events, respectively, with relative event intensity indicated by different marker sizes. Open circles indicate moderate ENSO events.

Figure 2 | Effect of total and anomalous currents on equatorial Pacific mixed layer heat balance during extreme El Niño and all La Niña events. **a**, Composite evolution of the interannual-scale mixed layer warming and cooling rates (color shades; in unit of °C per month) during extreme El Niño events (1982, 1997), with advection of temperature anomalies by the total current (arrow) removed. Red dashed and green lines indicate the altered slope β^* and the original β , respectively. **b**, As in **a** but for post-76 La Niña events. Only statistically significant values at the 95% confidence level are shaded in color, contoured, or marked by black arrows (gray arrows otherwise). β^* in **a** and **b** are respectively 0.55 and 0.69, both significant above the 95% confidence level ($P < 0.05$). **c**, As in **a** but with the effect of current anomaly removed. **d**, As in **c** but for La Niña. β^* in **c** and **d** are respectively 0.05 and -0.14, both not statistically significant ($P > 0.4$).

Figure 3 | Schematic of competing effects on zonal propagation direction during ENSO events. **a**, Zonal currents in the equatorial Pacific (large gray arrow) have the effect of shifting the initial warm surface anomalies (dashed red patch) eastward during extreme El Niño events, because the current anomaly u' (red arrow) is eastward and exceeds the strength of the westward background current \bar{u} (black arrow). This effect counters westward propagation as induced by the zonal advective and Ekman pumping feedbacks (blue arrow) and enhances eastward propagation induced by the thermocline feedback (pink arrow). **b**,

During La Niña events, the zonal currents are prominently westward as the current anomaly always enhances the westward flowing mean current. This weakens the thermocline feedback effect and enhances westward propagation as induced by the other two dynamical feedbacks.

Figure 4 | Statistics of El Niño occurrence characterized by prominent eastward propagation in CMIP3 and CMIP5 models. **a**, Probability density function (PDF) of 19 model ensemble mean in the past (1907-1999; blue) and future (2006-2098; red) periods. Each probability distribution is generated from 5000 bootstrap draws using the 19 model samples. The solid curves overlaid are the corresponding PDFs of a fitted normal distribution which are significantly different above the 95% confidence level ($P=0.01$). Dashed vertical lines indicate the corresponding ensemble average. **b**, Multi-model histogram for the event occurrence as a function of long-term averaged equatorial Pacific current velocity in the past (blue) and future (red) periods, segregated into bins of 0.04 m s^{-1} . **c**, As in **b** but segregated into bin size of 0.25 for the Niño3 index which is detrended and normalized by the standard deviation of the past period. **d**, As in **c** but stratified according to the concurrence with (thick dark bars) and without (thin light bars) current reversals. Dashed vertical line in **d** marks 1.5 unit of the normalized value.

METHODS

Heat budget analysis

We consider the heat balance of the surface mixed layer which can be expressed as follows:

$$T_t = -[(\bar{u} + u')T'_x + u'\bar{T}_x + \bar{w}T'_z + w'(T' + \bar{T})_z + (\bar{v}T')_y + v'(\bar{T} + T')_y] + Res. \quad (1)$$

The variables T , u , v , and w , are respectively potential temperature, zonal, meridional, and vertical ocean current velocities. Subscripts denote differential operators (x , y , z for zonal,

meridional, and vertical directions, respectively, and t for time). Prime and overbar denote anomalous and long-term averaged quantities, respectively. All variables are averaged between 5°S-5°N, over the surface layer depth of 50 m. The rate of change of the mixed layer temperature (T_t) is calculated as monthly increments using a centred-difference approximation. Terms not explicitly expressed in (1), such as eddy effects and damping by net air-sea heat fluxes, are absorbed into Res , such that the left and right hand sides of Equation (1) are identical. Equation (1) is slightly different to that adopted in previous studies^{8,20,21}, as $\bar{u}T'_x$ is expressed explicitly here and is viewed to interact with the non-linear advection term ($u'T'_x$). This combination, uT'_x , where $u = \bar{u} + u'$, is simply interpreted as the zonal advection of temperature anomalies by the total equatorial Pacific zonal current which can be readily observed. The term $\bar{u}T'_x$ tends to be overlooked as it is convolved into the continuity component via volume conservation [i.e., $T'(\bar{u}_x + \bar{v}_y + \bar{w}_z) = 0$] when the heat budget is expressed in flux form [i.e., $(\bar{u}T')_x + (\bar{v}T')_y + (\bar{w}T')_z$].

Quantification of propagation characteristic

The contour of $T_t=0$ marks the peak of T' , thus its positive (negative) slope in time-longitude space indicates eastward (westward) propagating T' (Figs. 1a, 1b). The phase transition slope, β , is calculated by fitting a line via least-square method to the contour between 160°E-80°W and May(0)-May(1) to allow some room for temporal movement upon removal of the advection terms. The rationale for the longitudinal extent can be found in the section below under the heading ‘Mean currents and ENSO propagation structures across models’, and our results are not sensitive to this aspect of the calculation.

Removing an important advection component from the right hand side of Equation (1) would alter the spatial and temporal structure of T_t , thus affecting β . For example, a reversal from a negative slope (i.e., westward propagation) to a positive (i.e., eastward) would suggest that

the component removed is crucial in setting the westward propagation. In this way, the role of a certain advection term on the propagation tendency of T' can be determined by comparing the altered slope β^* to the original β . The 95% regression standard error for the slopes is considered in all analysis by setting any slopes to zero if they are not greater than their corresponding error estimates.

Datasets and data processing

The reanalysis products utilised are ECMWF ORA-S3³¹, ECMWF ORA-S4³², SODA-2.16³³, SODA-2.2.4³⁴, and GODAS³⁵ (Supplementary Table 1). Each reanalysis system assimilates available observations (e.g., hydrographic profile data, moorings, satellites) into an ocean model forced by observed surface wind stress to calculate ocean currents. The reanalysis systems use different ocean models and data assimilation techniques. To focus on processes at ENSO time scales, a Butterworth low-pass filter³⁶ is applied prior to analysis to remove signals with periods shorter than 18 months. Without filtering, the spatio-temporal structure of the warming and cooling rate T_t is noisy given large high frequency monthly fluctuations. On ENSO time scales, the rate of warming and cooling tracks smoothly the evolution of SST anomalies.

ENSO classification and statistical significance test

The classification of ENSO events is based on the Niño3 index derived from the National Oceanic and Atmospheric Administration (NOAA) extended reconstructed SST version-3b³⁷, averaged over December-February when ENSO events typically peak. ENSO events are defined if the Niño3 amplitude, within each of the pre-76 (1959-1976) and post-76 (1976-2011) periods, is greater than 0.5 units of standard deviation. We classify these as strong if Niño3 exceeds 1 unit of standard deviation, and as moderate or weak otherwise. This yields

the following classification of events (developing phase year quoted): *Strong El Niño*: 1965, 1969, 1972, 1982, 1991, 1997, 2009; *strong La Niña*: 1970, 1973, 1975, 1988, 1998, 2007, 2010; *moderate El Niño*: 1963, 1976, 1987, 1994, 2002, 2006; *moderate La Niña*: 1964, 1967, 1984, 1995, 2005. The 95% statistical significance for each composite is evaluated using a bootstrap approach³⁸ in which samples of size N are randomly drawn repeatedly to obtain 1000 mean values. N is the number of ENSO events within each respective period pooled together for all the reanalysis products. All significance levels are evaluated based on the two-sided P -value.

Analysis of climate models

The observational analysis results demonstrate that, in the backdrop of the effects by the three ENSO dynamical feedbacks, the equatorial Pacific current is an important element for the zonal phase propagation of ENSO SST anomalies (Fig. 3). The observational-based results are further corroborated through an analysis of 40 CMIP3³⁹ and CMIP5⁴⁰ climate models (see Extended Data 5 for the specific models). The 40 models, each of 186 years in record (inclusive of the past and future simulations), provide a large sample of ENSO events that is about 180 times larger than the observed sample of 25 events. Thus, the models with their differences in the mean state provide a rigorous test bed for the effect of the current which along with the implications for the future are discussed in the following sections.

The past and future climate simulations respectively correspond to the 20th century (1907-1999) and future projection scenarios (2006-2098) based on Special Report on Emissions Scenarios (SRES) A1B for CMIP3 and representative concentration pathways (RCP) 4.5 for CMIP5^{39,40}. The time spans were necessarily chosen to include as many models as possible that cover the longest record without any missing data.

Mean currents and ENSO propagation structures across models

Based on the findings of early theoretical studies^{17,18} the prevalent direction of the basin-scale ENSO SST anomaly propagation along the equator is an indicator for the dominant dynamical process over a given epoch: net eastward for thermocline feedback and net westward for zonal advective/Ekman feedback. Such definition for the dominant ENSO dynamics has been adopted by previous studies^{41,42,43}, in which we term hereafter as ENSO ‘propagation structure’ to be in line with the topic of our study.

The diagnosis for ENSO propagation structure in observations and models has been achieved previously through a lead-lag correlation between the Niño3 index and an east-minus-west SST index which is taken as the difference between the Niño4, representing SST variability in the Central Pacific, and the Niño1+2 for the far eastern Pacific^{41,44}. The former is bounded in the west at 160°E and the latter in the east at 80°W, which is the exact longitudinal extent adopted in our study for calculating the phase transition slopes.

Here we diagnose the propagation structure in each past and future period in each model (Extended Data Fig. 5a) by the proportion of westward events (assigned as negative proportion) and eastward events (positive proportion) identified as El Niños and La Niñas with a statistically significant β . For each given period, the proportions of those four types of propagating events (i.e., westward El Niño and La Niña, and eastward El Niño and La Niña; the red/blue bars and lines in Extended Data Fig. 5a) and non-propagating events (non-statistically significant slopes) add up to 1, and so the net propagation structure (gray circles for 1907-1999; black triangles for 2006-2098) can range from -1, if all of the events propagate westward, to +1 if all propagate eastward. For example, the past ENSO events in model number 3 consist of 10% westward El Niños, 17% westward La Niñas, 28% eastward El Niños, 19% eastward La Niñas, and 26% non-propagating El Niños and La Niñas. Summing the proportions of the propagating events and considering the directions: -0.1 + -

0.17 + 0.28 + 0.19, yields an eastward propagation structure with a relative scale of 0.2 as marked by the gray circle. Although our approach is different to the commonly used correlation-based methods^{3,4,5}, in that we utilize β , the results using the two methods are largely consistent (figures not shown).

We find a significant positive inter-model correlation between ENSO propagation structure and mean equatorial currents (Extended Data Fig. 5b): models with weaker mean currents tend to generate a higher proportion of eastward propagating ENSO events, and the tendency is statistically significant. This suggests that models with weak (strong) mean currents tend to be more (less) favourable for the thermocline feedback resulting in an eastward propagation structure (as explained in Fig. 3). Some of the models that simulate too many eastward propagating La Niña events (Extended Data Fig. 5a; for example, models number 2, 3, 10, 17, 24, 25), in contrast to observations (but consistent with linear theories), tend to have a weak mean current. Because the inter-model correlation between the propagation structures and mean zonal wind stresses is basically zero (Extended Data Fig. 5c), such an effect is evidence for the direct influence of the ocean currents (e.g., related to specifications of the ocean model components), rather than, for instance, an effect of ENSO rectification onto the mean climate. These inter-model relationships also hold for the future simulations (see Extended Data Fig. 5 caption). While this result has an important implication for ENSO modelling, this in itself is evidence that the ocean current does have an influence on ENSO zonal phase propagation, that is, a weaker mean current is more favourable for eastward propagation.

The model ensemble results in Extended Data Fig. 5b also imply that in a climate state with a weak background current, natural variability alone (within which the system supports naturally varying ENSO propagation structure) would more easily produce eastward propagating events. With even weaker currents projected for the future, consistent with the

weaker Trade Winds, the thermocline feedback effect for inducing eastward propagation is favoured further (Extended Data Fig. 6). Previous ENSO stability analysis for a number of the CMIP3 models⁴⁵ demonstrated that the three main positive feedback processes are projected to increase, and would thus have competing effects on zonal phase propagation. The clear increase in the occurrences of eastward propagation events (Fig. 4a) can be more simply explained in terms of a weakened current as described in our study.

Effect of current reversals and models selection

One characteristic of the ENSO system is that the equatorial Pacific current anomaly is correlated with SST anomalies in the east (represented by the Niño3 index) in which the current leads Niño3 by about 3 months (Extended Data Fig. 4b). This highlights the tendency for an eastward (westward) current anomaly in boreal fall (September-December) to precede the peak of El Niño (La Niña) in boreal winter (December-February). A particularly strong eastward anomalous current was observed during the 1982/83 and 1997/98 extreme El Niños that leads to a re-intensified reversal in boreal fall, a feature not seen in other events (Extended Data Fig. 4a). These extreme events are identified by their prominent eastward propagation with phase transition slope β that is stronger than in other events (Extended Data Fig. 4d). Here we demonstrate using an aggregate of models that current reversals have an effect to make eastward propagation characteristic more prominent. Since zonal propagation is the focus of our study, and given the dynamical links of the aforementioned features, we first select the models based on the following criteria:

1. The models must be able to simulate at least one prominent eastward propagating El Niño event in either past or future simulation. Such event is defined as that when β is positive, greater than the linear-regression standard error, and is above 0.5 standard deviation unit of all El Niño slopes (i.e., following the observed counterpart; Extended Data Fig. 4d).

2. The models must be able to simulate at least one current reversal during boreal fall in either past or future simulation.
3. The models must produce a positive correlation between Niño3 and the current during any propagating El Niño events, a relationship also seen in observations (Extended Data Fig. 4c).

These criteria result in 24 models that simulate more realistic and distinctive current evolution between strong and moderate El Niño years (Extended Data Fig. 8) as expected from observations (Extended Data Fig. 4a), in contrary to that in the discarded models (Extended Data Fig. 9).

The effect of current reversal on zonal phase propagation is clearly exhibited by this aggregate of models, that is, to favour eastward propagation. This is due to the fact that the corresponding β tends to be more positive whenever the events coincide with a current reversal (Extended Data Fig. 7b). In the case where current reversals coincide with westward propagation, the westward slopes are found to be substantially weaker. Such an effect renders a positive correlation between the total current and β (Extended Data Fig. 7a), which is a characteristic also seen in observations (Extended Data Fig. 4d). This positive correlation further highlights the crucial role of the equatorial Pacific current on zonal phase propagation.

The effect of the total current on El Niño and La Niña propagation asymmetry is also reproduced (Extended Data Fig. 7c). The asymmetry becomes apparent with strong El Niño events, and more so when these co-occur with current reversals, similar to the observed counterpart (Fig. 2a, b; Supplementary Table 4).

An additional criterion is applied, resulting in a further exclusion of 5 models. Each of these excluded models already simulates 11 to 14 El Niño events with prominent eastward propagation slope over the 93 years in the past simulation (Extended Data Fig. 10a). These

are too frequent relative to the 2 events over the 53 years of observational record, which translates to slightly less than 4 events for the 93 model years. The remaining 19 models simulate from none up to 8 events (i.e., double the expected observed frequency) in the past period. These 19 models also have climatological states that roam the regime of westward propagation structure similar to the observed, as opposed to the 5 excluded models that tend to cluster about the eastward regime with already weak mean currents (Extended Data Fig. 5b; models number 8, 17, 24, 25, 29). Given the extreme rarity, and to test whether a change in model climatological state can induce increased occurrence of such events, we retain the 19 models for future projections (Fig. 4).

Future projection: a parallel with the late 20th Century scenario

With the mean westward currents projected to weaken in the future (Extended Data Fig. 6), thus providing a more conducive condition for increased occurrences of current reversals (Extended Data Fig. 7d), it is expected that there will be more El Niño events exhibiting prominent eastward propagation characteristic in the future.

A 100% increase in the mean occurrence of such events is found (Fig. 4a), with 16 out of 19 models projecting an increase. Considering only models that simulate less than 8 events increases this to more than 116%, with model consensus consistently above 83%. As expected, retaining those that already simulate frequently occurring events (i.e., saturated with eastward propagation) reduces the amount of increase to 76% when including models that already simulate of up to 11 events, and 46% using all of the 24 models. Nonetheless, in all cases, the models as an aggregate simulate a notable increase in future occurrences of eastward propagating El Niño events that is significant well above the 95% confidence level, with at least 75% of the models projecting an increase.

543 As revealed by the observational analysis, the emergence of an eastward propagation in the
544 post-76 period is in part because the mean westward current is weaker, and in part because
545 the eastward current anomalies associated with the extreme El Niños are sufficiently large to
546 reverse the current. On this regard, the variety of events and mean states provided by the
547 different models point to a slightly different scenario for the future in which the importance
548 of the projected current weakening is highlighted. This is evident as the model consensus is
549 weak in the projection for stronger ENSO amplitude (11 out of 19 models; Extended Data Fig.
550 10c), but all of the models project a weaker mean current (Extended Data Fig. 10b). Despite
551 this, there is still a tendency for stronger increase in the number of eastward propagating
552 events in models that also project a larger increase in ENSO amplitude (Extended Data Fig.
553 10c). This is through the contribution by current reversals (Extended Data Fig. 10d) which
554 tend to occur with stronger El Niño and have an effect in making the eastward propagation
555 characteristic more prominent (Extended Data Fig. 7).

556 It is necessary to note that while weaker mean current facilitates current reversal, such that
557 any modest eastward current anomaly can more easily exceed the background current, the
558 increase in the number of current reversals in the future (Extended Data Fig. 7d) do not
559 always translate to more occurrences in events having a prominent eastward propagation
560 characteristic (Extended Data Fig. 10d). This is expected given the various kinds of event
561 concurrences that the model aggregate provides (Extended Data Fig. 7). In fact, while all of
562 the increase in eastward propagating events is associated with weaker mean currents and El
563 Niño events of all magnitude (Figs. 4b and c), only 45% of this is associated with current
564 reversal events, within which 85% are associated with large magnitude El Niño events (Fig.
565 4d).

Thus, given the weak model consensus in projecting an increase in ENSO amplitude, the most robust feature shared between the future projection and the change observed during the late 20th Century is the weaker westward mean current which is projected by all of the models.

Methods references

31. Balmaseda, M. A., Vidard, A., & Anderson D. The ECMWF ocean analysis system: ORA-S3. *Mon. Wea. Rev.* **136**, 3018–3034 (2008)
32. Balmaseda M.A., Mogensen, K. & Weaver, A. Evaluation of the ECMWF Ocean Reanalysis ORAS4, *Quarterly Journal Roy. Met. Soc.*, doi: 10.1002/qj.2063, In press (2013).
33. Carton, J. A. & Giese, B. S. A reanalysis of ocean climate using simple ocean data assimilation (SODA). *Mon. Wea. Rev.* **136**, 2999-3017 (2008).
34. Giese, B. S. & Ray, S. El Niño variability in simple ocean data assimilation (SODA), 1871-2008. *J. Geophys. Res.* **116**, C02024, doi:10.1029/2010JC006695 (2011).
35. Behringer, D. W. The Global Ocean Data Assimilation System at NCEP. *11th Symposium on Integrated Observing and Assimilation Systems for Atmosphere, Oceans, and Land Surface*, AMS 87th Annual Meeting, Henry B. Gonzales Convention Center, San Antonio, Texas, 12pp. (2007).
36. Roberts, J. & Roberts, T. D. Use of the Butterworth low-pass filter for oceanographic data. *J. Geophys. Res.* **83**(C11), 5510-5514 (1978).
37. Smith, T. M., Reynolds, R. W., Peterson, T. C. & Lawrimore, J. Improvements to NOAA's historical merged land-ocean surface temperature analysis (1880–2006). *J. Climate* **21**, 2283–2296 (2008).
38. Efron, B. & Tibshirani, R. J. *An Introduction to the Bootstrap* (Chapman & Hall, 1993)

39. Meehl, G. A., et al. The WCRP CMIP3 Multimodel Dataset: A New Era in Climate Change Research. *Bull. Amer. Meteor. Soc.* **88**, 1383–1394 (2007).
40. Taylor, K. E., Stouffer, R. J., & Meehl, G. A. An Overview of CMIP5 and the Experiment Design. *Bull. Amer. Meteor. Soc.* **93**, 485–498 (2012).
41. Guilyardi, E., El Niño-mean state-seasonal cycle interactions in a multi-model ensemble. *Clim. Dyn.* **26**, 329–348 (2006).
42. Santoso, A., England, M., & Cai, W. Impact of Indo-Pacific feedback interactions on ENSO dynamics diagnosed using ensemble climate simulations. *J. Climate* **25**, 7743–7763 (2012).
43. Aiken, C. M., Santoso, A., McGregor, S., & England, M. H. The 1970's shift in ENSO dynamics: A linear inverse model perspective. *Geophys. Res. Lett.* **40**, doi:10.1002/grl.50264 (2013).
44. Trenberth, K. E., & Stepaniak, D. P. Indices of El Niño Evolution. *J. Climate*, **14**, 1697–1701 (2001).
45. Kim, S.-T., & Jin, F.-F.: An ENSO stability analysis. Part II: results from the twentieth and twenty-first century simulations of the CMIP3 models. *Clim. Dyn.* **36**, 1609–1627 (2011).

Extended Data Figure legends

Extended Data Figure 1 | Zonal propagation of SST anomalies and effect of current on mixed layer heat balance during ENSO events. **a**, SST³⁷ anomalies along the equatorial Pacific (averaged between 5°S-5°N) over January 1959 to December 2011, with seasonal cycle and linear trend (referenced to the entire 1959-2011) removed. The arrows, whose slopes are calculated from the multi-reanalysis ensemble average, indicate zonal propagation directions. **b**, Composite evolution of interannual-scale heating rate (color shades; in unit of °C per month) of the equatorial Pacific mixed layer during post-76 moderate El Niño events. The phase transition (dashed black line) tracks the evolving peak of temperature anomaly (red and blue contours; red for positive and blue for negative) with a statistically significant linear fit slope (green line; $\beta = -0.97$, $P < 0.01$). **c**, As in **b** but with advection due to the total current (arrow) removed, resulting in $\beta^* = -0.29$ (red dashed line) that is statistically significant ($P < 0.05$). Only statistically significant values above the 95% confidence level are shaded in color, contoured, or marked by black arrows (gray arrows otherwise). **d**, As in **c** but for extreme El Niño events (1982, 1997) with the effect of mean current (arrows) removed. **e**, As in **d** but for post-76 La Niña events. The β^* values are 1.44 in **d** and 0.61 in **e** which are statistically significant ($P < 0.01$).

Extended Data Figure 2 | Time evolution of equatorial Pacific zonal current and wind stress. **a**, The same as Fig. 1c for zonal current velocity averaged across the reanalysis products. The dashed curve highlights interdecadal variation using a 13-year running mean. Gray shading denotes two standard deviation about each mean value, representing monthly spread and variations across reanalyses. **b**, As in **a** but for surface zonal wind stress.

Extended Data Figure 3 | Time evolution of the equatorial Pacific zonal current across reanalysis products. Raw time series of zonal current velocity averaged over 5°S-5°N, 160°E-90°W, capturing the Niño4 to Niño3 regions, and over the ENSO development phase (August to December). The ensemble average (1980-2006) is marked by the thick horizontal dashed line.

Extended Data Figure 4 | Observed characteristics of equatorial Pacific current associated with ENSO. **a**, Total current evolution composited over developing phase of ENSO: extreme El Niño (dark red shading/black line), strong El Niño (red shading/dark red line), weak El Niño (pink shading/red line), and La Niña (blue shading/dark blue line). Thick lines indicate the mean composites, and the colored shades are for one standard deviation unit above and below the means representing the spread across the different reanalyses and each classified events. **b**, Lead-lag monthly correlation between the reanalysis ensemble average current and Niño3 with eastward current anomalies leading warm Niño3 anomalies at 3 months. **c**, Total current averaged over September to December versus Niño3 (December-February) associated with extreme (dark red circles), strong (red circles), and weak (green circles) El Niño events in each pre and post-76 period, with a correlation coefficient of 0.82, significant at 99% level. Open circles indicate non-statistically significant β . The correlation ($r=0.84$) remains significant at 99% level even when these points are excluded. **d**, As in **c** but for total current versus β during all ENSO events (blue circles for La Niña). The correlation coefficient between current and statistically significant β for El Niño is $r=0.75$ which is significant at 99% level. The dashed horizontal line in **d** marks 0.5 standard deviation unit of all the El Niño slopes.

Extended Data Figure 5 | ENSO propagation structure in CMIP models. **a**, Propagation structure in each CMIP model (gray circles for 1907-1999; black triangles for 2006-2098

period) and observations (1959-2011; large open circle). The propagation structure is defined by summing up the proportion of westward events (negative proportion) and eastward events (positive proportion) identified as El Niño (red bar for 1907-1999; red line for 2006-2098) and La Niña (blue bar for 1907-1999; blue line for 2006-2098) with statistically significant β . The different color intensities for the bars and lines contrast the four types of propagating events. The proportions of propagating events and non-propagating events add up to 1, and so the net propagation structure (gray circle or black triangle) can range from a scale of -1, if all events propagate westward, to +1 if all propagate eastward. Eastward (westward) propagation structure is an indication for a more dominant thermocline (zonal advective) feedback mechanism. **b**, Propagation structure versus long-term annually averaged zonal current velocity across all CMIP models (colored markers) in the past simulation, revealing a positive correlation ($r=0.40$) significant at 95% level ($r=0.44$ for future). Open circle marks the observed counterpart using data from 1959 to 2011 for a larger event sample. **c**, As in **b** but for mean zonal wind stress, exhibiting no significant correlation ($r=0.01$; $r=0.14$ for future). Models marked by dotted horizontal lines in **a**, and squares in **b** and **c**, indicate those selected for future projections (Fig. 4). Models marked with diamonds in **b** and **c** simulate realistic flow features but are saturated with eastward propagating events that they already produce in the past simulation (see Extended Data Fig. 10a).

Extended Data Figure 6 | Projected changes of long-term mean zonal wind stress, zonal current velocity, and propagation structure across the CMIP3 and CMIP5 models. a, Future and past difference in long-term mean zonal wind stress and zonal current velocity. **b**, Future and past difference in long-term mean zonal wind stress and ENSO propagation structure (Extended Data Fig. 5). **c**, Future and past difference in long-term mean zonal current velocity and ENSO propagation structure. The correlations between each of the

variables are shown in the panels and are statistically significant at the 99% level. Removing the model outlier (miroc3-2-hires) reduces correlations in **a**, **b**, and **c**, to 0.61, 0.47, 0.59, respectively, but are still statistically significant up to the 99% level.

Extended Data Figure 7 | Effect of current reversals on zonal phase propagation and

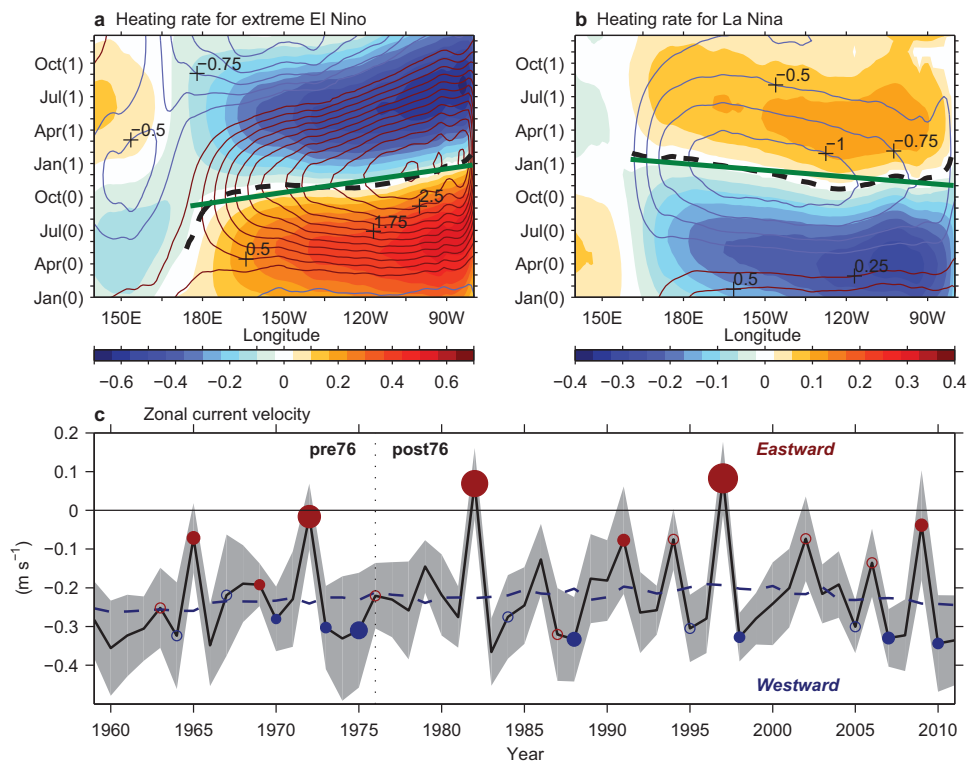
future projection. The analysis incorporates the 24 models that simulate realistic flow features (see Methods). **a**, Correlation between total current and phase transition slope during El Niño events in the past simulation (1907-1999). The positive correlation ($r=0.46$), significant above the 99% level (with 472 data points), confirms the relationship seen in the limited observational record (Extended Data Fig. 4). **b**, Probability density of β for westward (gray) and eastward (red) El Niño events with (darker shading) and without (lighter shading) current reversals. **c**, Probability density of the difference in phase transition slope before and after the effect of total current removed from the heat balance ($\beta-\beta^*$), for all La Niña (blue), all El Niño (light red), and El Niño events that co-occur with current reversals (darker red). The probability density for strong El Niño events (greater than 1 standard deviation) is shown by dashed curve. **d**, Probability density of number of current reversals associated with any events in the past (1907-1999; blue) and future (2006-2098; red) periods. Vertical lines in **d** indicate the respective mean values (6.4 and 9.5 for past and future periods, respectively). The statistics in **b**, **c**, and **d** are generated using bootstrap sampling technique with 5000 simulations.

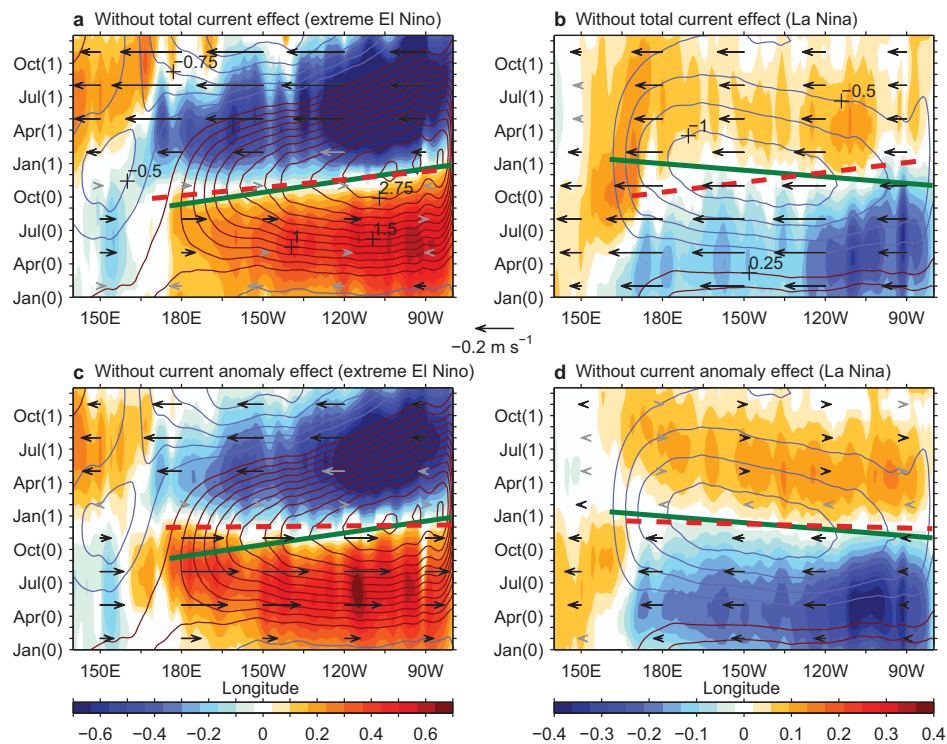
Extended Data Figure 8 | Monthly evolution of the total current during developing year of El Niño events in the selected CMIP3 and CMIP5 models. Red and gray curves respectively represent El Niño events in both past and future simulations that are classified as above and below 1.5 standard deviation unit of Niño3 (December-February average)

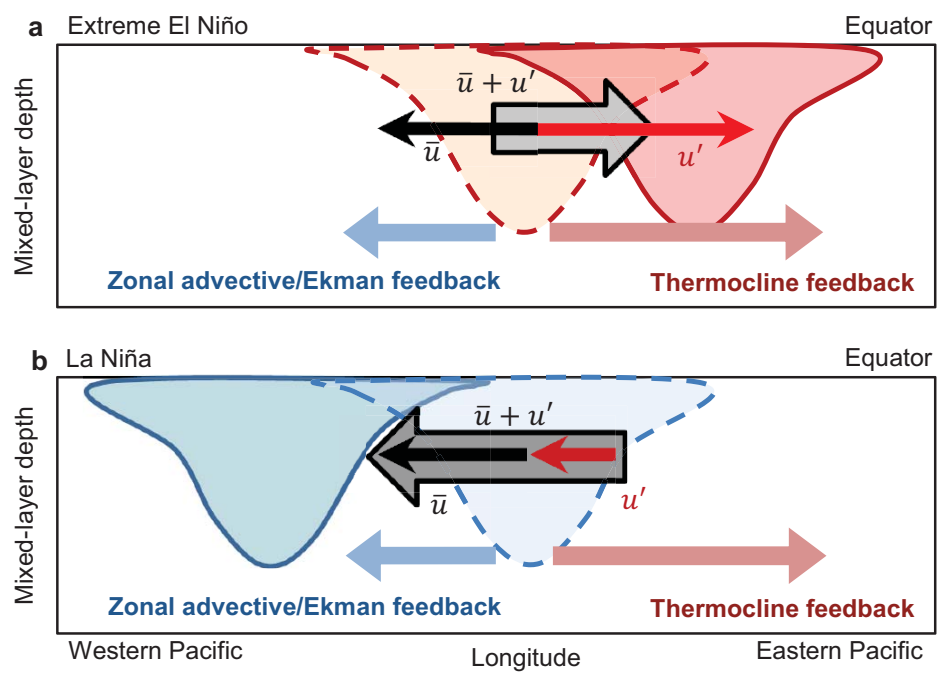
normalized by the standard deviation of the past period. Only events with statistically significant transition slopes are considered. The corresponding dashed curves indicate the sample averages. Each panel displays the correlation coefficient between the equatorial Pacific current (September - December average) and the Niño3 anomalies, following the observed counterpart (Extended Data Fig. 4c).

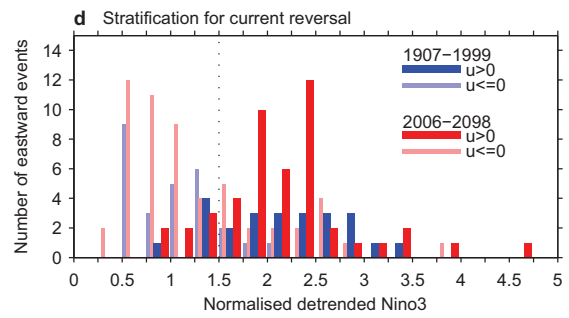
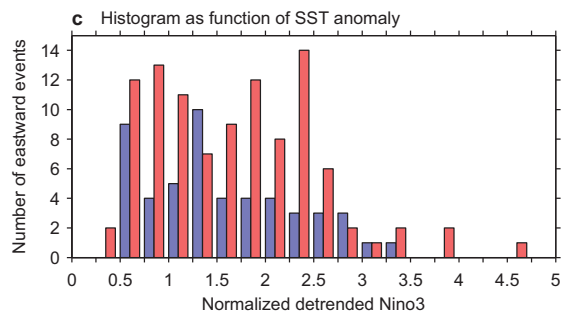
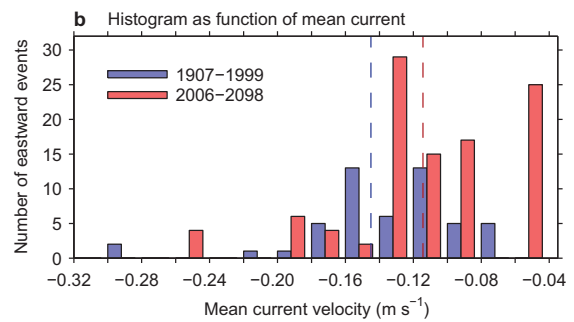
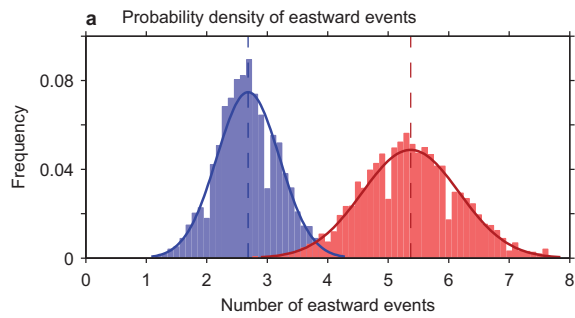
Extended Data Figure 9 | As Extended Data Fig. 8, but for the excluded models. Correlation coefficients displayed in red are not statistically significant.

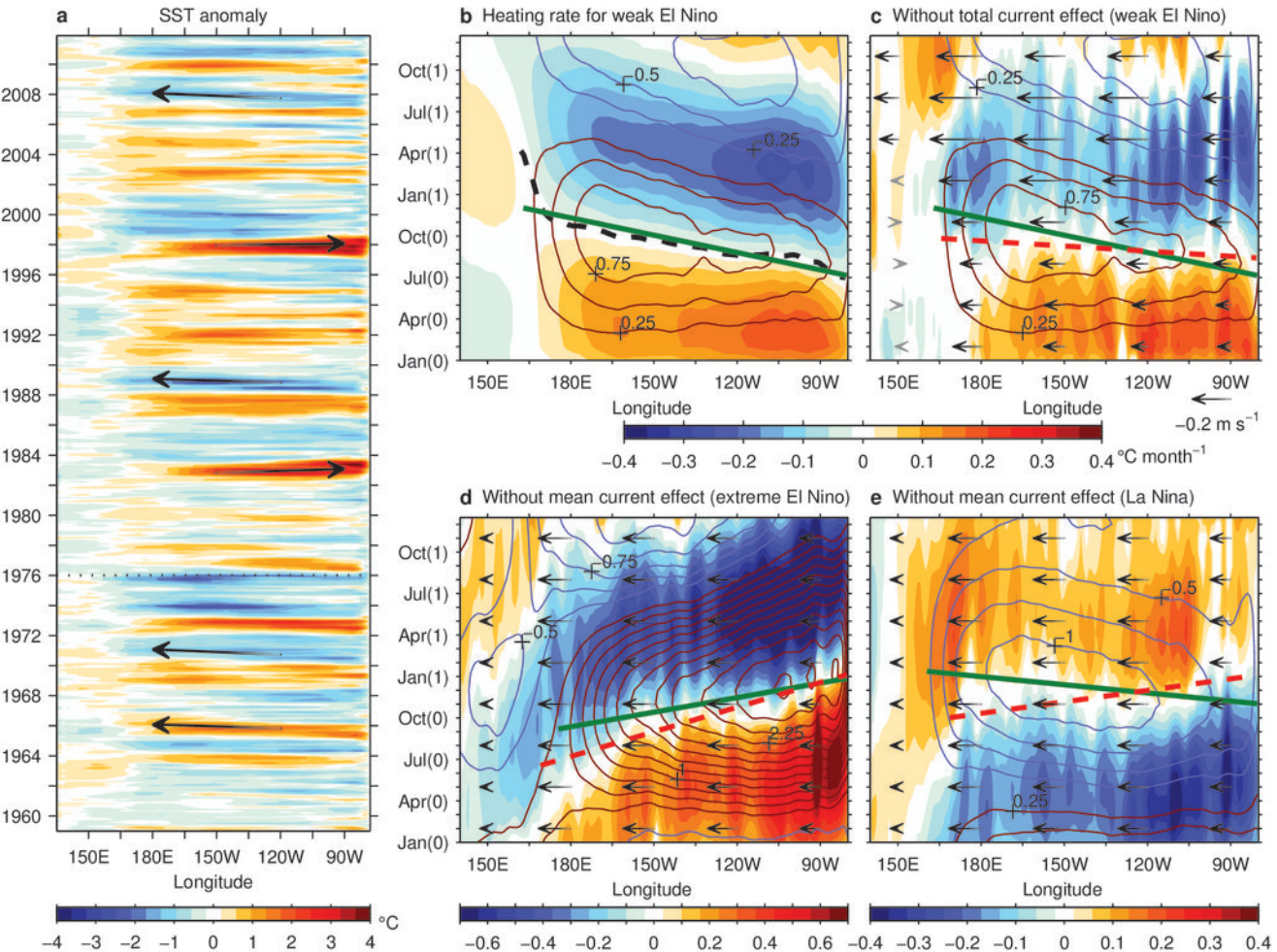
Extended Data Figure 10 | Occurrences of El Niño with prominent eastward propagation and future projection as a function of mean current, ENSO amplitude, and current reversals in the CMIP3 and CMIP5 models. **a**, Number of events for each of the 40 models for the past (1907-1999; blue) and future (2006-2098; red) periods (see Methods for event criteria). The number of events over the 93 model years expected from the observed occurrences is 4 (dotted vertical line). For future projection, we consider models that produce occurrence of none up to 8 events (i.e., doubling; dashed vertical line). Dotted horizontal lines indicate the selected models. **b**, Future and past difference in event occurrences against that of the long-term mean zonal current velocity. **c**, As in **b** but against the future and past difference in ENSO amplitude as defined by the standard deviation of Niño3 index. **d**, ENSO amplitude difference against the difference in number of eastward propagating events with current reversals. The correlation coefficients displayed in the panels are significant at 95% level.



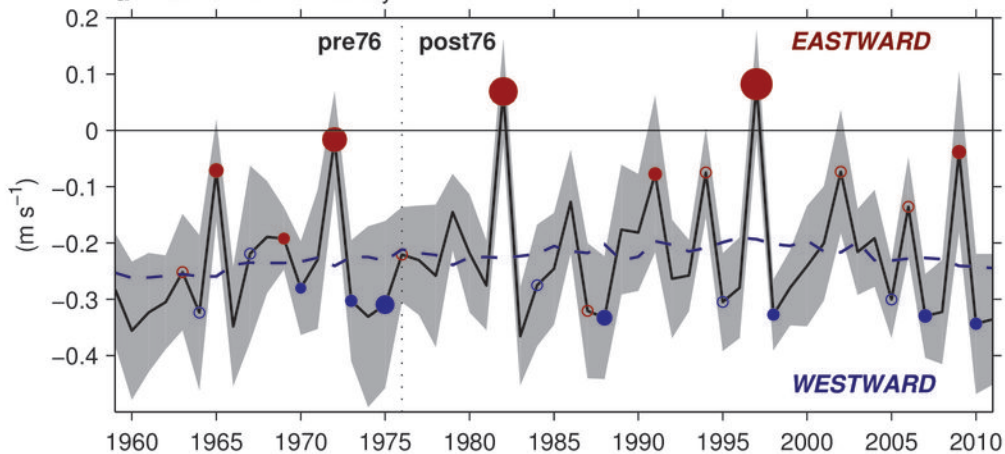




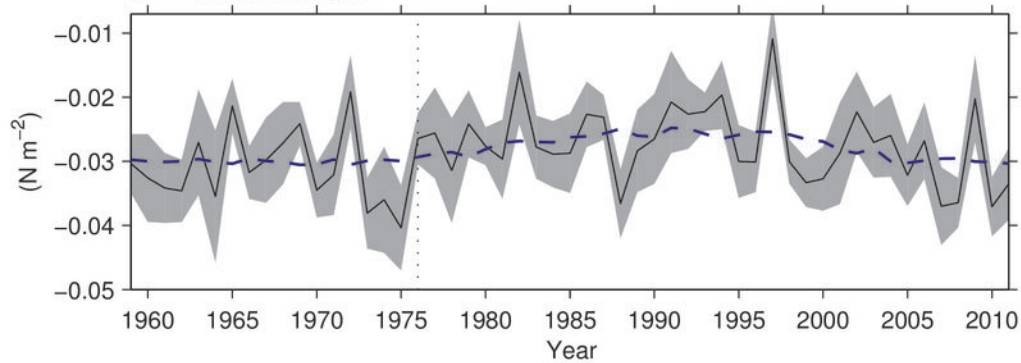


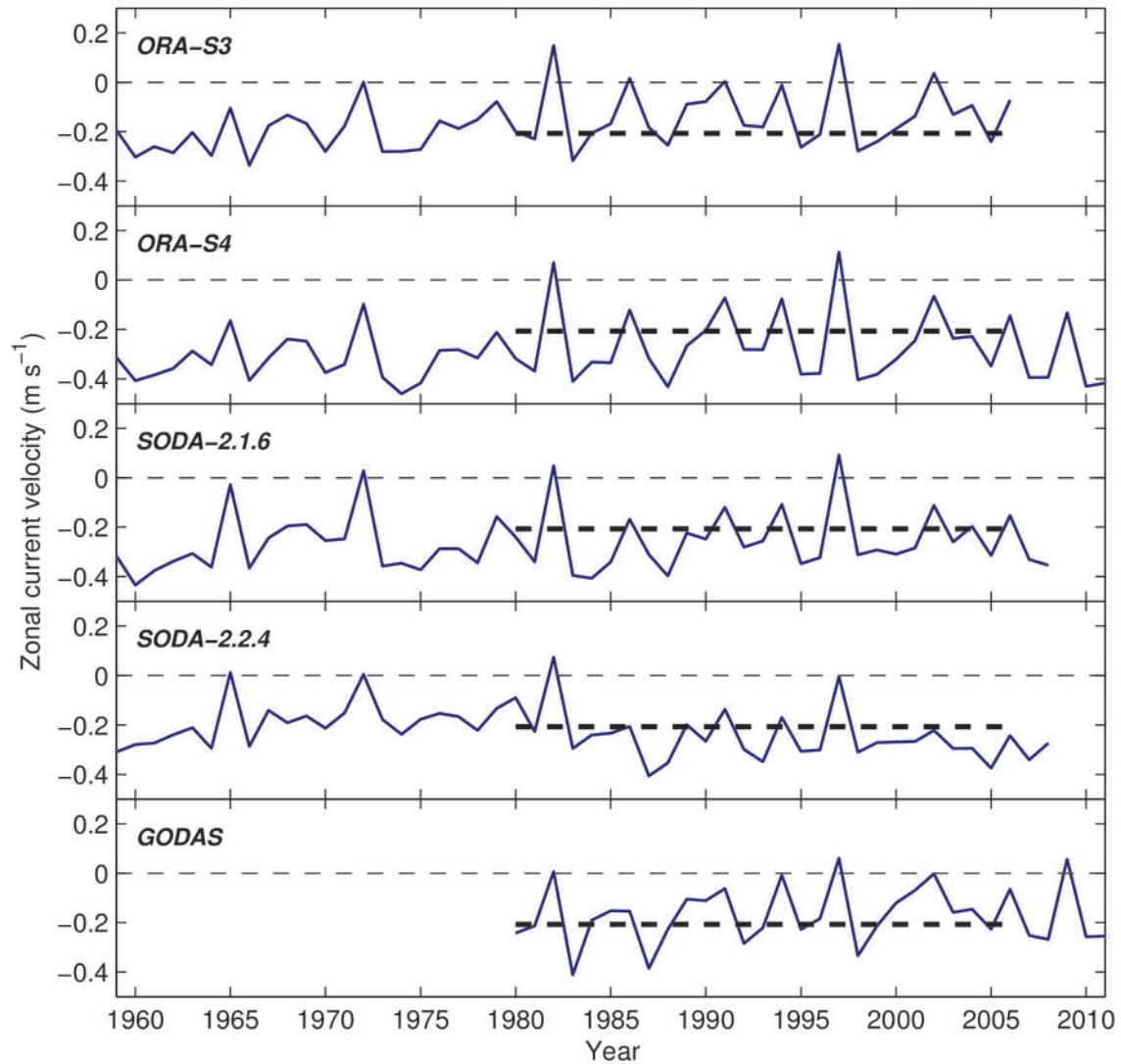


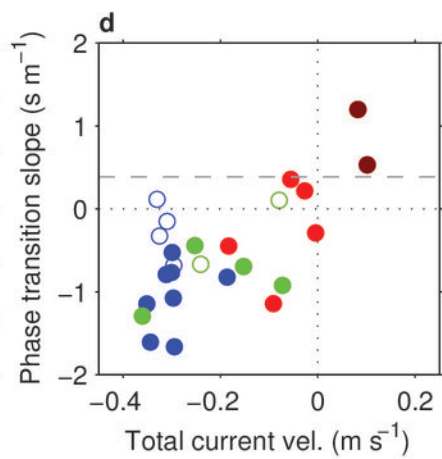
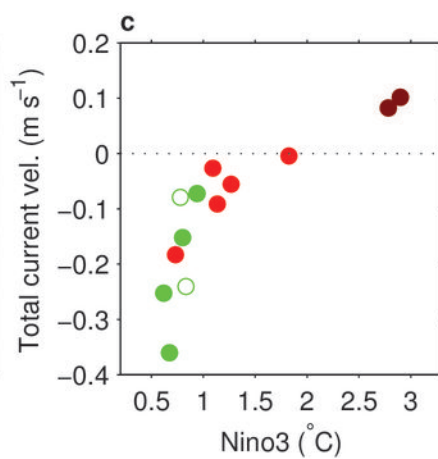
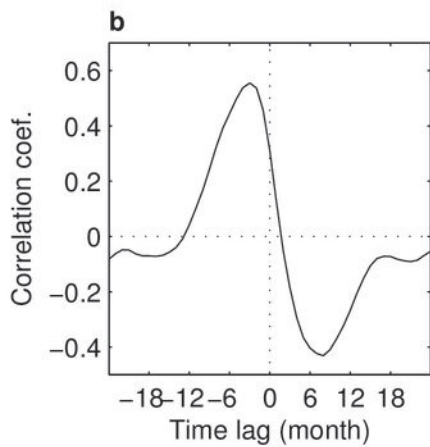
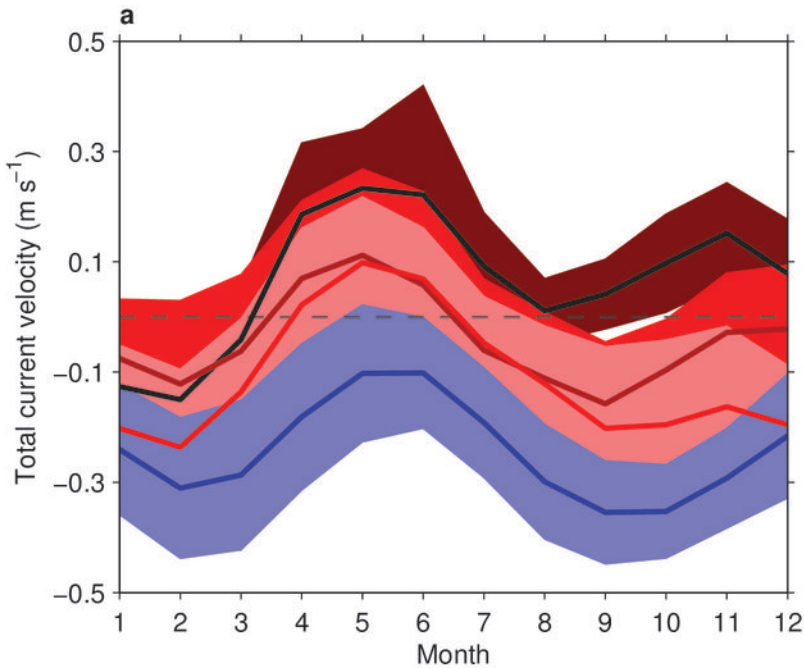
a Zonal current velocity

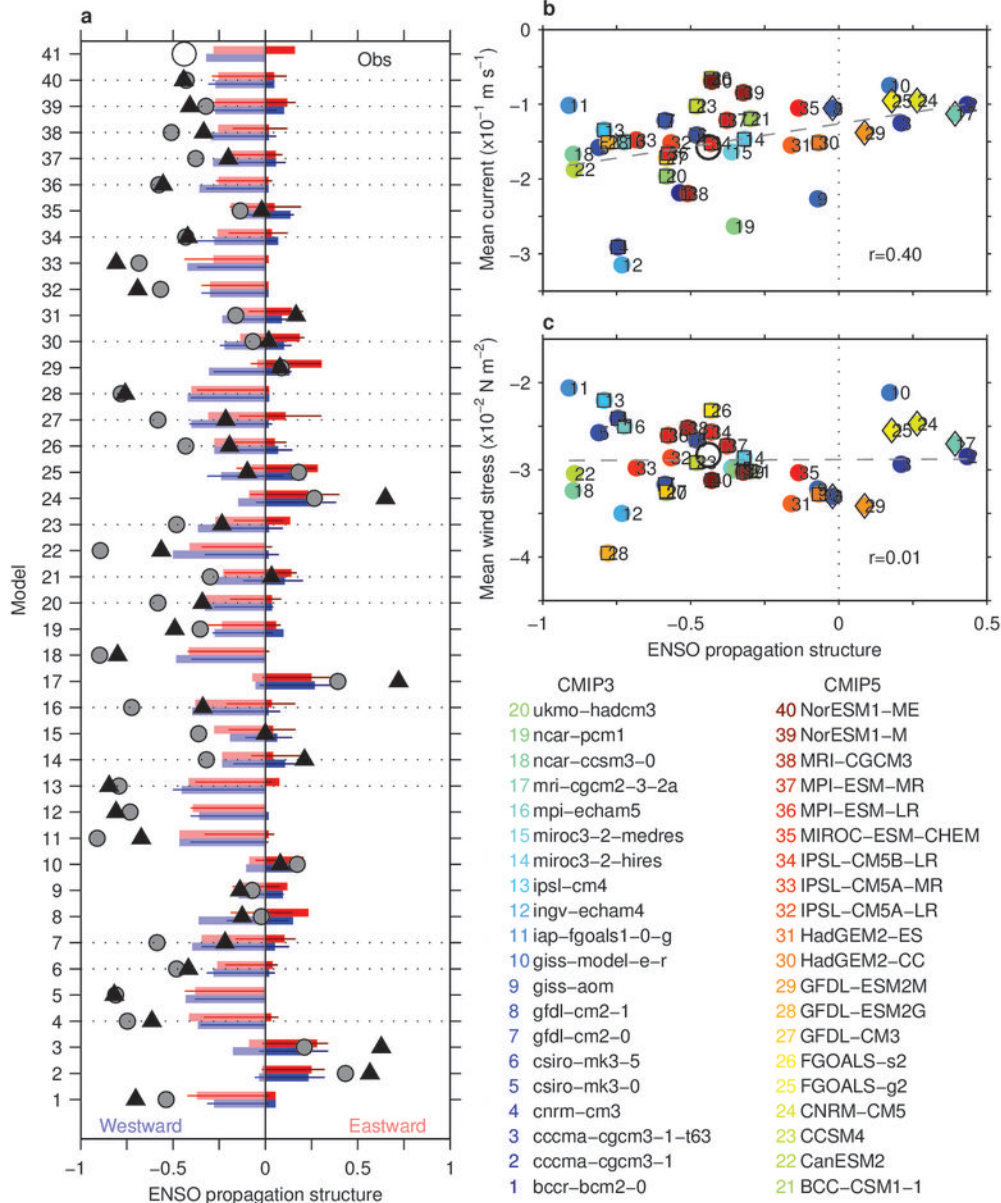


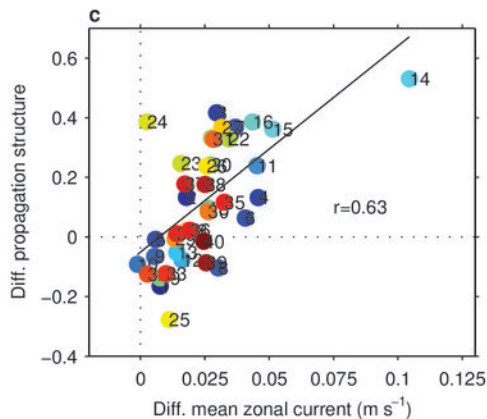
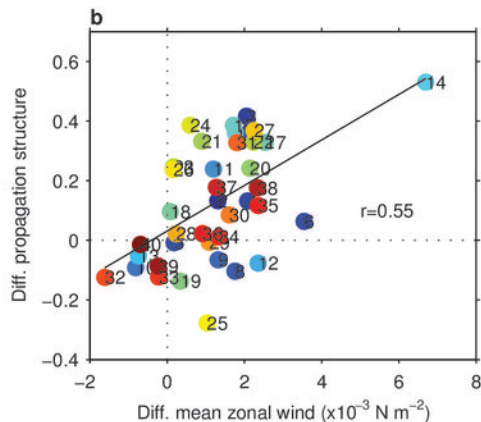
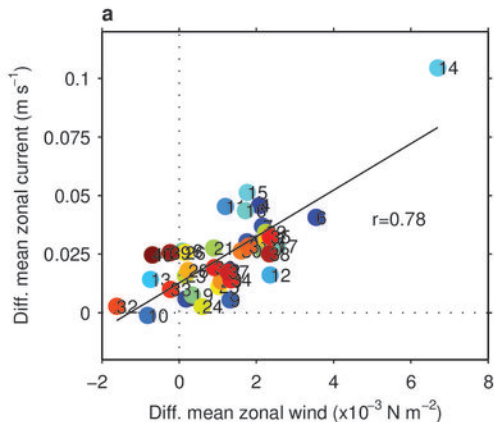
b Zonal wind stress



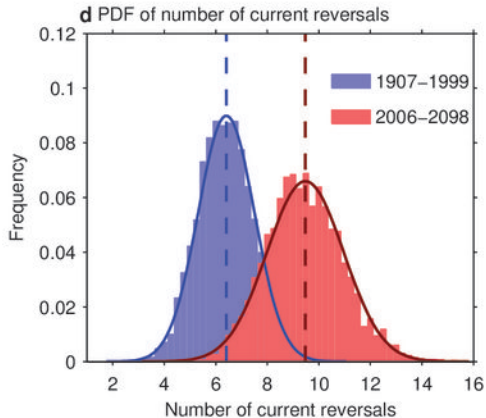
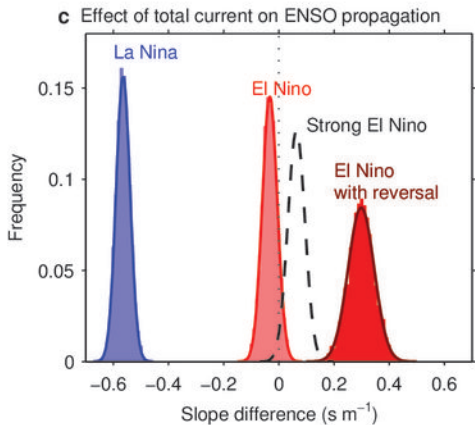
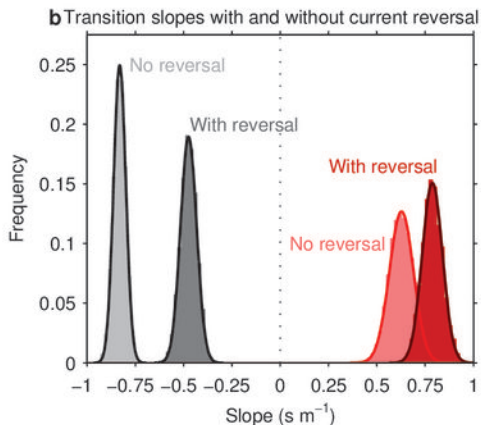
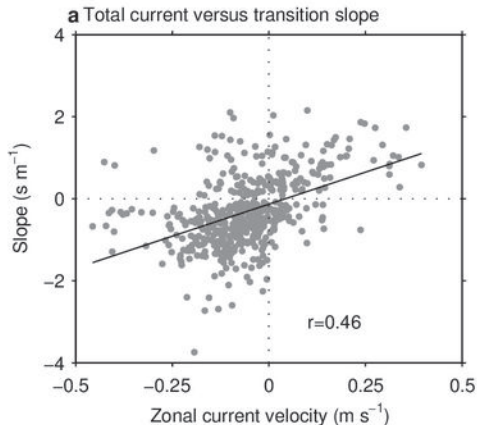


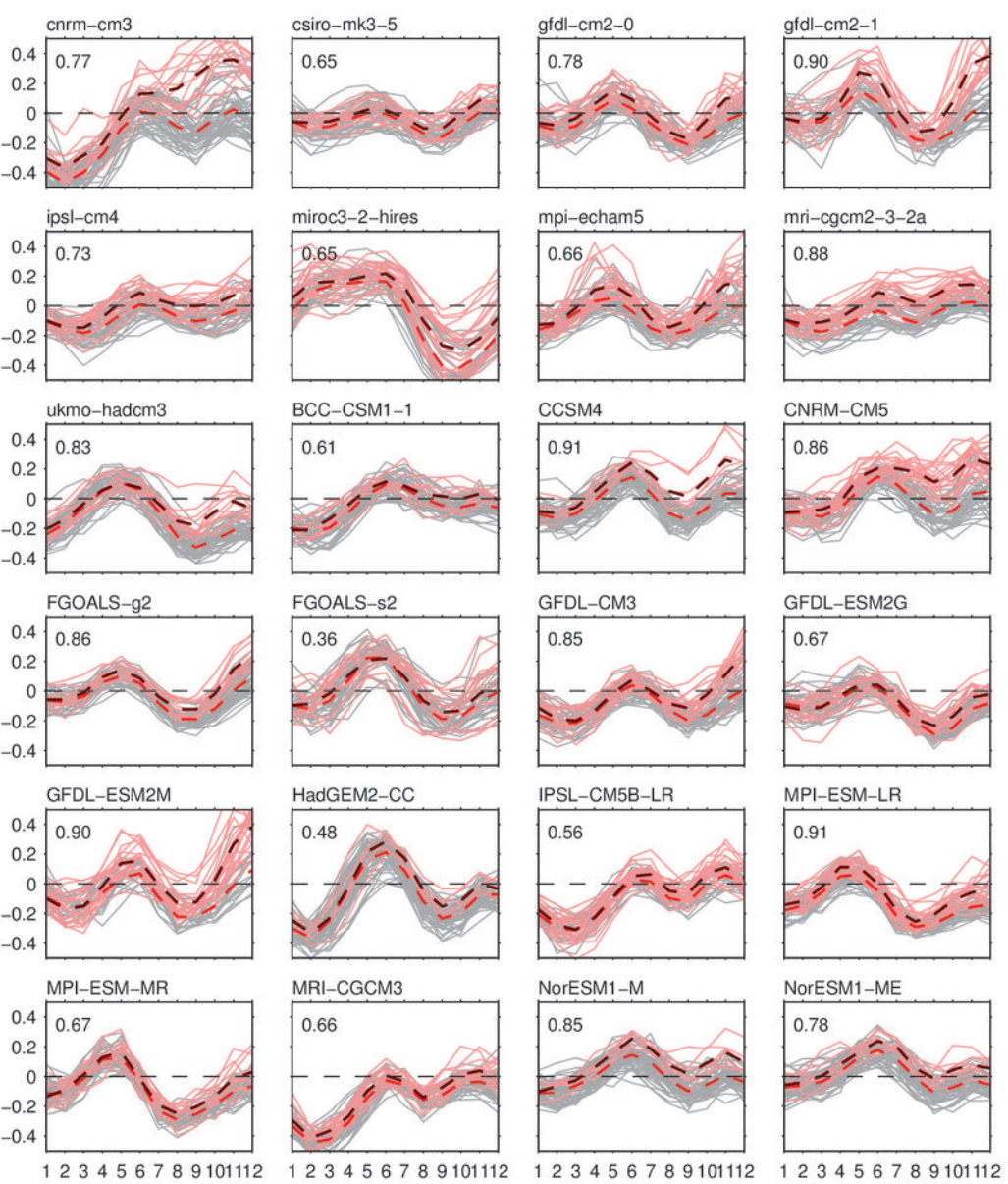


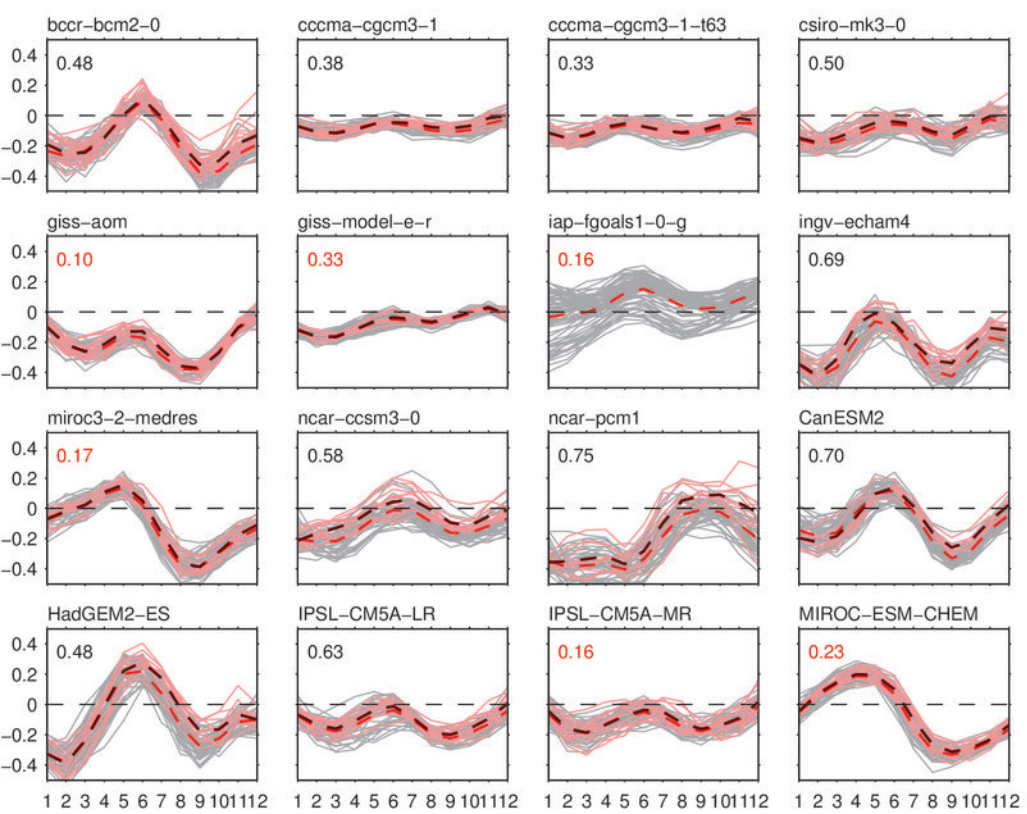


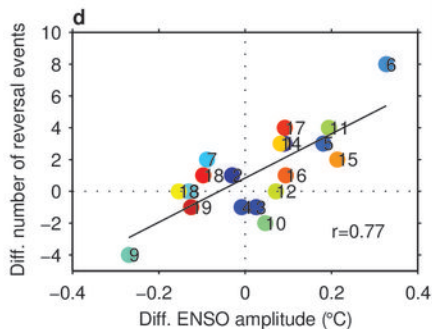
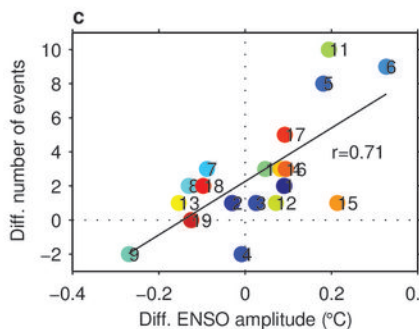
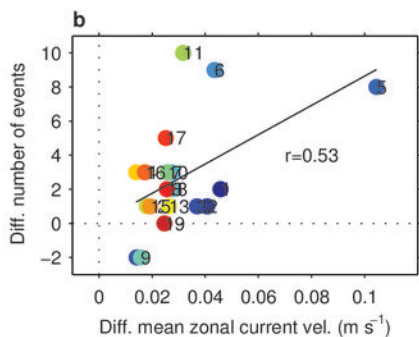
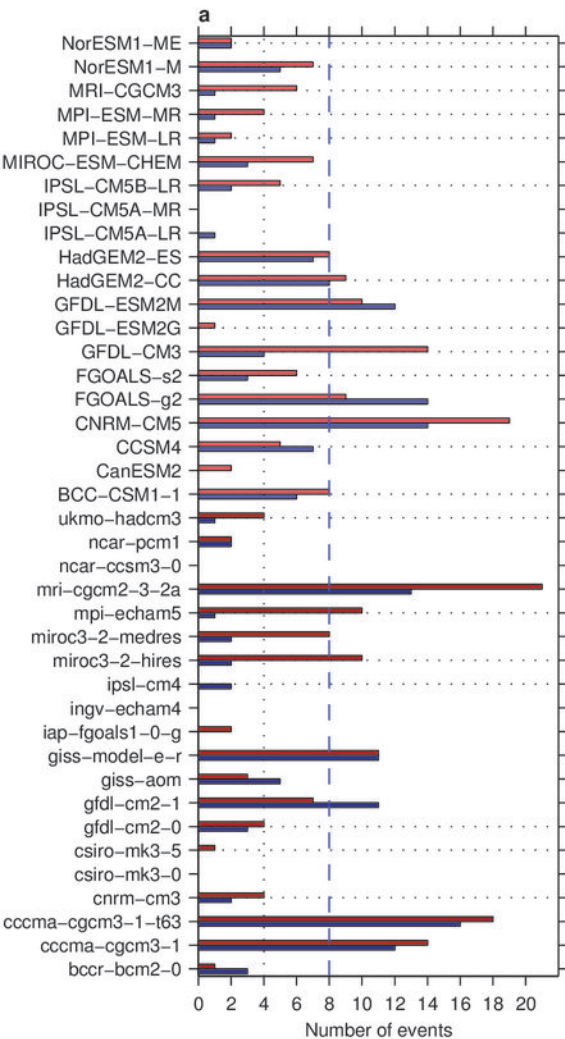


- | | |
|---------------------|-------------------|
| 20 ukmo-hadcm3 | 40 NorESM1-ME |
| 19 ncar-pcm1 | 39 NorESM1-M |
| 18 ncar-ccsm3-0 | 38 MRI-CGCM3 |
| 17 mri-cgcm2-3-2a | 37 MPI-ESM-MR |
| 16 mpi-echam5 | 36 MPI-ESM-LR |
| 15 miroc3-2-medres | 35 MIROC-ESM-CHEM |
| 14 miroc3-2-hires | 34 IPSL-CM5B-LR |
| 13 ipsl-cm4 | 33 IPSL-CM5A-MR |
| 12 ingv-echam4 | 32 IPSL-CM5A-LR |
| 11 iap-fgoals1-0-g | 31 HadGEM2-ES |
| 10 giss-model-e-r | 30 HadGEM2-CC |
| 9 giss-aom | 29 GFDL-ESM2M |
| 8 gfdl-cm2-1 | 28 GFDL-ESM2G |
| 7 gfdl-cm2-0 | 27 GFDL-CM3 |
| 6 csiro-mk3-5 | 26 FGOALS-s2 |
| 5 csiro-mk3-0 | 25 FGOALS-g2 |
| 4 cnrm-cm3 | 24 CNRM-CM5 |
| 3 cccma-cgcm3-1-t63 | 23 CCSM4 |
| 2 cccma-cgcm3-1 | 22 CanESM2 |
| 1 bccr-bcm2-0 | 21 BCC-CSM1-1 |









- 19 NorESM1-ME
- 18 NorESM1-M
- 17 MRI-CGCM3
- 16 MPI-ESM-MR
- 15 MPI-ESM-LR
- 14 IPSL-CM5B-LR
- 13 HadGEM2-CC
- 12 GFDL-ESM2G
- 11 GFDL-CM3
- 10 FGOALS-s2
- 9 CCSM4
- 8 BCC-CSM1-1
- 7 ukmo-hadcm3
- 6 mpi-echam5
- 5 miroc3-2-hires
- 4 ipsl-cm4
- 3 gfdl-cm2-0
- 2 csiro-mk3-5
- 1 cnrm-cm3